Submitted to Materials Science and Engineering A (April 2020): revised May 2020

The fabrication of high strength Zr/Nb nanocomposites using high-pressure torsion

Dan Luo[a,*], Teodor Huminiuc[b], Yi Huang[b,c,*], Tomas Polcar[b], Terence G. Langdon[b]

[a] Department of Materials Science and Engineering, The University of Sheffield, Sheffield S1 3JD, UK

[b] Engineering Materials, Department of Mechanical Engineering, University of Southampton, Southampton SO17 1BJ, UK

[c] Department of Design and Engineering, Faculty of Science and Technology, Bournemouth University, Poole, Dorset BH12 5BB, UK

Abstract

Nanocomposites of Zr/Nb with exceptionally high hardness were fabricated successfully through the high-pressure torsion (HPT) processing of prepacked Nb/Zr/Nb sandwich samples at ambient temperature. The initial layers of Nb and Zr became fragmented during HPT processing with the formation of many fine-scale intermixed Zr/Nb layers. The intermixing of these Zr/Nb layers increased both with increasing HPT revolutions from 10 to 100 and with increasing radial positions on the disks. The Vickers microhardness, Hv, increased with increasing revolutions and with radial position reaching a maximum of ~700 Hv at the edge of the 100 turns sample. Exceptional grain refinement to the range of ~20 to 40 nm and the occurrence of twinning were associated with the HPT-processed Zr/Nb composites after 100 turns. These results suggest a potential route for fabricating high strength bulk Zr/Nb nanocomposites.

Keywords: hardness; high-pressure torsion; nanostructures; ultrafine grains; Zr/Nb nanocomposites

***Corresponding authors:** Dan Luo (d.luo@sheffield.ac.uk), Yi Huang (yhuang2@bournemouth.ac.uk)

1. Introduction

In order to enhance the mechanical properties of metals, various elements may be mixed in a controllable way to form composite structures [1-3] and the mixture can then be tuned so that the required properties of the composite are enhanced and may even surpass the properties of the comprising elements [2, 4]. In recent years, bimetallic composites have attracted considerable attention as they exhibit enhanced strength, hardness and plastic properties even under extreme conditions as well as resistance to shock and radiation damage compared to the constituent materials in bulk form. Examples of these composites include Al/Cu, Cu/Nb, V/Ag, etc. [5–12].

To date, most of the research interest in metallic composites has focused on using combinations of crystal structures of bcc/fcc, fcc/fcc and bcc/bcc materials [13–19] but recently there has been an interest in developing cubic/hcp combinations [20–25]. Considering the Zr/Nb system, it is well-known that zirconium and zircalloys are widely employed in the nuclear industry due to their small capture cross-section for thermal neutrons, their relatively good high temperature strength and their resistance to corrosion [26]. Therefore, it is reasonable to anticipate that Zr/Nb bimetallic nanoscale composites may be promising candidate materials for use in the nuclear industry due to the development of intrinsic highly efficient interfaces which will protect these materials against radiation damage [27, 28].

Metallic composites of this type are generally obtained by using deposition methods such as magnetron sputtering [29] and already there is a report of the preparation of Zr/Nb nano-multilayers using this procedure [26]. Nevertheless, the relatively low deposition rate and the overall complexity of the equipment that is needed for this synthesis technique make this type of processing difficult for the fabrication of large volumes of material. Mechanical alloying (MA) is also a potential approach for preparing these composites [5] but a simpler and more direct procedure is through the use of a severe plastic deformation (SPD) technique such as

high-pressure torsion (HPT) where this procedure is now routinely used to produce bulk nanostructured metallic materials [30]. Processing by HPT has been employed recently to produce nanostructured intermetallics and metal matrix composites and the results have shown that the procedure provides the potential for achieving true nanostructures [31–35]. Non-equilibrium phases, such as supersaturated solid solutions [36], may be formed using this procedure and the resultant mechanical properties are enhanced due both to the significant grain refinement and to the intensive introduction of point and line defects during processing [37].

An earlier report described the fabrication of a Zr/Nb composite using two semi-circular sections of a disk which were placed together to form a single whole disk within the HPT facility [5]. Processing by HPT produced an ultrafine-grained structure with grain sizes of less than 100 nm and a supersaturated solid solution with a hardness of up to 500 Hv at the disk edge after 100 turns of HPT [5]. In practice, most reports on the fabrication of bulk Zr/Nb composites have used the technique of accumulative roll bonding (ARB) [38-41] and very limited information is at present available on the effect of heavy shear strains on the fabrication of bulk Zr/Nb composites when using the HPT technique. Furthermore, the early study using HPT produced a Zr/Nb composite by taking two semi-circular disks [5] and this is similar to early reports for other materials using two semi-circular disks [42] or four quarter disks [43], respectively. More recent experiments have been conducted differently by stacking whole disks in a sandwich-like configuration [31] where this procedure provides a better opportunity for evaluating the significance of mixing during the HPT process.

The only report on the HPT processing of a Zr/Nb composite available to date has limitations due to the necessity of cutting semi-circular Zr and Nb disks [5]. Accordingly, the present research was initiated to develop a novel and compact approach for making Zr/Nb composites by stacking Nb/Zr/Nb disks in a sandwich-like structure for the HPT processing. Therefore, a comprehensive investigation was conducted to examine the production,

microstructure and the microhardness of an Zr/Nb composite after processing at room temperature. The results demonstrate the potential for using HPT for the fabrication of nanocomposites having exceptionally high levels of hardness.

2. Experimental material and procedures

The materials used in this study were commercial purity Zr and Nb rods purchased from Goodfellow (Cambridge, UK). Both the as-received Zr and Nb rods were in an annealed state. Disk-shaped samples with diameters of 9.9 mm and thicknesses of 0.85 mm were cut from the as-received Zr and Nb rods. A Zr disk was stacked on the lower anvil of the HPT facility contained between two Nb disks in a sandwich-like configuration where both the upper and lower anvils had central depressions with diameters of 10 mm and depths of 0.25 mm, respectively. Representative schematic illustrations of the HPT configuration are available in several earlier reports [31, 44, 45]. These piled disks were processed by quasi-constrained HPT in which there is a small outflow of material around the periphery of the disk during processing [46,47]. Following conventional practice, the Nb/Zr/Nb disks were piled in the depression on the lower anvil without any glue or the application of any metal brushing treatment to the disk surfaces [32]. All HPT processing was performed at room temperature under a compressive pressure of 6.0 GPa using a rotation speed of 1 rpm for revolutions of 10, 20, 50, 80 and 100 turns, respectively.

Following HPT, each HPT-processed disk was cut vertically along the diameter using a diamond wafering saw to provide two semi-circular disks. The emerging microstructures were then characterized on the overall cross-sections using both an optical microscope (OM) and a scanning electron microscope (SEM) equipped with an energy dispersive spectrometer (EDS) analyzer. The values of the Vickers microhardness (Hv) were measured on the polished cross-sectional surfaces at intervals of 0.15 mm along the diameters and at intervals of 0.1 mm along the vertical thickness using an FM-300 microhardness tester with a load of 200 g (equivalent

to 1.96 N) and dwell times of 15 s. Color-coded contour maps were constructed from the hardness data to display the distributions of the hardness values on the cross-sectional planes of each HPT-processed disk. Samples for transmission electron microscopy (TEM) were extracted using a FEI Helios focused ion beam (FIB) and they were analyzed by TEM using an image-corrected FEI Titan microscope operating at 300 kV and a JEOL 2100 STEM.

3. Experimental results

Fig. 1 shows OM images of the cross-sectional areas of the Nb/Zr/Nb stacks after processing through 10, 20, 50, 80 and 100 turns, respectively. These images provide clear evidence for the gradual evolution of a nanocomposite. Initially there is a layered structure of Nb/Zr/Nb after 10 turns in Fig. 1(a) with the two elements well-defined in the image. As the numbers of turns increases to 20, as shown in Fig. 1(b), the initial layered structure becomes fragmented close to the disk edge but an area of distinct Nb/Zr/Nb layers remains visible in the central area of the disk. This shows that there is an intermixing of the Zr and Nb fragments at the disk edge area even after only 20 turns. For 50 turns in Fig. 1(c), the outer regions near the edge show intermixed microstructures of Nb and Zr whereas, at higher magnifications, fine scale Zr/Nb layers are visible in the disk centre area over distances of ~1 mm on either side of the midpoint of the disk. With further increases in rotation to 80 and 100 turns, the intermixed microstructure gradually becomes more homogenous in both the central and edge areas with well-defined mixed microstructures of Nb and Zr as shown in Figs 1(d) and (e).

Representative SEM micrographs are shown in Fig. 2(a,b) for the polished cross-sections near the edge and centre of the Zr/Nb composite fabricated by HPT through 50 turns and with EDS mapping of the elements in the central regions shown in Figs 2(c,d). The edge and centre appear differently in the micrographs because most of the edge area has a smooth surface in Fig. 2(a) whereas in the disk central area there is an uneven surface roughness and evidence for fine-scale lamellae in Fig. 2(b). The EDS maps at the centres in Figs 2(c) and (d) confirm

that the uneven surface roughness and fine-scale lamellae are related to the presence of fine-scale Zr/Nb layers. This contrasts with the disk edge area where the smooth surface corresponds to a good mixture of Zr and Nb.

Values of the Vickers microhardness were measured on the polished cross-sectional surfaces of each sample after HPT processing and the results are shown in the form of color-coded contour maps in Fig. 3 for samples processed through 10, 20, 50 and 100 turns, respectively. For 10 turns, the micro-hardness values are ~200 - 300 Hv with a layered hardness distribution along the thickness direction which is due to the initial Nb/Zr/Nb layered microstructure (Fig. 1(a)). After 20 turns the hardness is ~200 - 350 Hv at $0 < r < 3.0$ mm but with hardness values of ~300 – 400 Hv at $r > 3.0$ mm where r is the radius at each position. Increasing to 50 turns, the hardness increases to ~250 - 350 Hv at $r < 3.0$ mm and to ~350 - 450 Hv at larger radii. Finally, for 100 turns the hardness lies between ~300 - 400 Hv at $r < 3.0$ mm but increases to ~700 Hv close to the edge of the disk.

In order to study the variation in grain size in the central region with different numbers of turns, as well as to identify any differences in microstructure between the central and edge areas, HPT-processed Zr/Nb nanocomposites were analyzed using TEM in the central and edge areas. Fig. 4 shows bright field (BF on left) and dark field (DF on right) images of the HPT-processed samples for the central regions after (a,b) 80 and (c,d) 100 turns and for the edge region (e,f) after 100 turns. It is evident that the DF images highlight certain grains by allowing transmission of only scattered parts of the beam.

To obtain quantitative information on the microstructural development during HPT processing, grain sizes were measured from TEM images with at least 400 grains counted for each sample. The upper row in Fig. 5 shows the selected area electron diffraction (SAED) patterns associated with the central areas after (a) 80 and (b) 100 turns and (c) at the edge after 100 turns and the lower row in (d-f) shows plots of the grain size distributions for these same

three conditions, respectively. Thus, the grain refinement process is highlighted where the characteristic SAED patterns evolve from the 80 turns sample where there is a relatively larger grain set of reflections to the highly-strained 100 turns diffractogram at the edge. In the latter case, the presence of a continuous ring pattern confirms there are a large number of small crystallites which are randomly oriented as shown in more detail in Fig. 5(c) The grain size distributions in Fig. 5(d-f) were calculated using the equivalent circle method. Two main features are noted from these histogram plots in Fig. 5(d-f): (a) there is a constant increase in the numbers of small grains measuring between ~20 to 40 nm laterally and (b) there is a narrowing in the distributions with increasing numbers of turns and also with the radial position within the disk sample.

Fig. 6 shows high resolution (HR) and fast Fourier transform (FFT) pattern images of the edge of the 100 turns sample for (a) the bcc Nb and (b) the twinned hcp Zr. The cubic structure of Nb is more stable when subjected to the HPT process and, as a result, there is a higher unit cell symmetry while the hcp Zr forms twin boundaries along the [2-1-12] crystalline plane. Fig. 7 shows the EDS elemental mapping after 100 turns for the specimens extracted from (a) the central region and (b) the edge. It is concluded that the severely deformed samples show uniform concentrations of both component elements and the atomic ratio of Nb:Zr is calculated as lying between 2.2:1 and 2.6:1. There is also no noticeable difference between the 80 and 100 turns samples in terms of the elemental compositions.

4. Discussion

In the HPT procedure, a disk is processed under a high compressive pressure with concurrent torsional straining and this is generally, but not always, conducted at room temperature. In practice, the large hydrostatic pressure which is an inherent feature of HPT processing is effective in leading to the successful processing of difficult-to-deform materials [48] that may be prone to segmentation and cracking when processing using other SPD

techniques [49, 50]. The physical and mechanical characteristics are almost invariably enhanced by the production of significant grain refinement and the intensive introduction of point and line defects [37].

In HPT processing, the shear strain is not introduced homogeneously but instead a disk is subjected to a shear strain, γ, which is given by a relationship of the form [51]

$$\gamma = \frac{2\pi Nr}{h} \tag{1}$$

where N, r and h are the numbers of HPT revolutions and the radius and thickness of the disk, respectively. The torsional straining imposed within the disk is therefore dependent upon the distance from the centre and the strain is theoretically zero when r = 0.

From eq. (1) it is reasonable to anticipate that inhomogeneities will occur in both the microstructure and the hardness within disks subjected to HPT processing. Nevertheless, experiments show that HPT disks gradually develop a reasonable hardness homogeneity with increasing numbers of turns [52] and this has been effectively explained using strain gradient plasticity modeling [53]. Therefore, in the present investigation, the initial layered microstructure is well-defined after 10 turns in Fig. 1(a) and with increasing straining from 20 to 100 turns the microstructure gradually becomes more mixed and more homogeneous from the edge to the centre, especially after 80 and 100 turns. Fig. 2 provides confirmation that there is greater mixing, and the material becomes more homogeneous, from the edge to the centre.

Recently, experimental observations on two phase materials such as duplex stainless steel [54-57] demonstrated that double-swirl flow patterns form on the HPT disk surface and finite element modelling depicted the development of turbulent eddy flows within the sample cross-sections during the processing [58-61]. Therefore, in addition to the in-plane shear strain, there is also mass transfer within the samples in HPT and this assists in the redistribution of metal components in the metal-metal composite and consequently in the formation of striations. The most recent example is the layered structure developed in an immiscible Cu-Ta alloy processed

by HPT [62]. In the present research at low numbers of HPT turns, as shown in Fig. 1, the disk edge has good mixing of the Nb-Zr layers due to the large shear strains whereas in the disk centre area striations of Nb-Zr layers are visible due to the reduced shear strain. As the number of HPT turns increases, the difference between the disk centre and the edge gradually diminishes.

After 100 turns in this research the hardness in the vicinity of the edge areas was ~700 Hv. It is now well-established that different strengthening mechanisms with various microstructural modifications may exist in HPT processing [31,63]. In the present investigation a nano-structure was formed after 80 and 100 turns and the grains became increasingly refined with increases in the numbers of HPT revolution and the radial position on the disk. Therefore, there was a gradient in grain refinement along the radius of the disk which is directly attributed to the increase in shear strain due to torsional straining as shown in eq. (1). It is expected, therefore, that the disk-shaped samples will have a radial gradient of crystallization and the hardness will increase with increasing radius according to the appropriate grain boundary strengthening mechanism so that high hardness is achieved at the outer edge. The radial increase in strength is supported by the observed nanostructural modifications of the fine bi-metallic granular structure which promotes the formation of dislocation barriers under increased torsional stresses. The results in Fig. 5 show that the distributions of grain sizes become more homogeneous with increasing numbers of turns and also with the radial position on the disk-shaped sample.

Most of the earlier investigations of bulk Zr/Nb bimetal composites were conducted using ARB and focused primarily on microstructural development, either through the grain size or texture, with relatively little attention devoted to the mechanical properties **[**38–41**]**. Research on Zr/Nb bimetal composites produced by different approaches mainly focused on the nano-mechanical behavior [26] whereas the present investigation provides comprehensive

information on the microhardness of these samples after large numbers of turns. Specifically, the results show the microhardness may reach ~700 Hv at the edge of the 100 turns sample and this is much higher than the values reported for pure Zr, pure Nb, Zr–Nb alloys, Zr/Nb composite and other different systems after processing by HPT where the maximum microhardness values are not higher than ~500 Hv [5, 32, 33, 36, 64-69].

For convenience, Table 1 shows the maximum Vickers hardness values reported for several different systems after HPT processing with a special emphasis on Zr and/or Nb. This tabulation confirms the exceptional hardness achieved in the present investigation for the Zr/Nb nanocomposite.

It is important to note that in the early experiments where two semi-circular disks of Zr and Nb were placed to form a whole disk and then processed by HPT at room temperature under a pressure of 5 GPa, the maximum hardness at the outer edge after 100 turns was reported as ~500 Hv [5]. This demonstrates that mixing becomes easier and the microstructural evolution is more rapid when placing disks in the HPT facility in a sandwich-like configuration. In the HPT processing in the present research there was evidence for twinning in the Zr lattice and this is important because twinning plays a significant role in the plastic deformation of hcp metals and alloys due to the limited number of operating slip systems [6]. Furthermore, it was reported that the microhardness can be improved with increasing areal fraction of twins since the twin boundaries act as barriers to the movement of dislocations [7]. By contrast, the earlier report using semi-circular disks described the formation of a supersaturated solid solution after 100 turns but without any evidence for the occurrence of twinning [5]. These results show, therefore, that twinning may provide an important contribution towards the strengthening of Zr/Nb composites.

The EDS mapping shown in Fig. 7 demonstrates the final relatively uniform concentrations of both component elements after 100 turns which has evolved from an initial

Nb/Zr/Nb layers. It is apparent that the HPT processing is extremely effective in mixing the initial layered structure of the composite material and thereby improving the mechanical properties of the Zr/Nb composite. Therefore, the improved mechanical properties obtained in this research is attributed to a combination of the formation of a nanostructured material and the occurrence of twinning.

5. Summary and conclusions

1. By using a sandwich-like stacking of Nb/Zr/Nb disks, a Zr/Nb composite was successfully fabricated using processing by high-pressure torsion at ambient temperature. Processing through 100 turns of HPT gave a fully-mixed Zr/Nb composite with a large fraction of grains lying in the range of ~20-40 nm.

2. The intermixing of the Zr/Nb layers increased with increasing numbers of imposed revolutions from 10 to 100 turns and with increasing radial position on the disks. After 100 turns, the material was essentially fully-mixed.

3. Microhardness measurements showed that the hardness increased preferentially in the edge region of the disk and after 100 turns the hardness at the edge was measured as ~700 Hv. This is an exceptionally high hardness for a Zr/Nb composite and the high hardness is attributed to a combination of the formation of a nanostructured array of grains and the occurrence of twinning by the HPT processing.

Acknowledgements

This work was supported by the European Research Council under ERC Grant Agreement No. 267464-SPDMETALS. The electron imaging was performed with the support of the South of England Analytical Electron Microscope (EP/K040375/1) within the David Cockayne Centre for Electron Microscopy, Department of Materials, University of Oxford. Additional support was provided by the Henry Royce Institute (EP/R010145/1) and CEITEC Nano Research Infrastructure (ID LM2015041, MEYS CR, 2016–2019) and CEITEC Brno

University of Technology, Czech Republic. One of the authors (YH) thanks the QR fund from Bournemouth University.

Data Availability

The raw/processed data required to reproduce these findings cannot be shared at this time as the data also forms part of an ongoing study.

References

[1] M. Azimi, M.R. Toroghinejad, M. Shamanian, J Mater Sci 53 (2018) 12553–12569.

[2] M. Kawasaki, S.H. Jung, J.M. Park, J. Lee, J.I. Jang, J.K. Han, Adv. Eng. Mater. 22 (2019) 1900483(1-9).

[3] C. Ding, J. Xu, X. Li, D. Shan, B. Guo, T.G. Langdon, Adv. Eng. Mater. 22 (2020) 1900702(1-12).

[4] M.M. Castro, S. Sabbaghianrad, P.H.R. Pereira, E.M. Mazzer, A. Isaac, T.G. Langdon, R.B. Figueiredo, J. Alloys Compd. 804 (2019) 421–426.

[5] T. Miyazaki, D. Terada, Y. Miyajima, C. Suryanarayana, R. Murao, Y. Yokoyama, K. Sugiyama, M. Umemoto, Y. Todaka, N. Tsuji, J Mater Sci 46 (2011) 4296–4301.

[6] I.J. Beyerlein, A. Caro, M.J. Demkowicz, N.A. Mara, A. Misra, B.P. Uberuage, Mater. Today 16 (2013) 443–449.

[7] R. Uscinowicz, Compos Part–B Eng. 55 (2013) 96–108.

[8] A.H. Assari, B. Eghbali, J. Alloy Compd. 773 (2019) 50–58.

[9] A. Bellou, L. Scudiero, D. F. Bahr, J Mater Sci 45 (2010) 354–362.

[10] W.Z. Han , A. Misra, N.A. Mara, T.C. Germann, J.K. Baldwin, T. Shimada, S.N. Luo, Phil. Mag. 91 (2011) 4172–4185.

[11] Q.M. Wei, N. Li, N. Mara, M. Nastasi, A. Misra, Acta Mater. 59 (2011) 6331–6340.

[12] L.F. Zeng, P. Fan, L.F. Zhang, R. Gao, Z.M. Xie, Q.F. Fang, X.P. Wang, D.Q. Yuan, T. Zhang, C.S. Liu, J. Nucl. Mater. 508 (2018) 354–360.

[13] A. Misra, J.P. Hirth, R.G. Hoagland, Acta Mater. 53 (2005) 4817–4824.

[14] Y. Chen, Y. Liu, C. Sun, K.Y. Yu, M. Song, H. Wang, X. Zhang, Acta Mater. 60 (2012) 6312–6321.

[15] M.A. Monclús, M. Karlik, M. Callisti, E. Frutos, J. LLorca, T. Polcar, J.M. Molina-Aldareguía, Thin Solid Films 571 (2014) 275–282.

[16] R. Raghavan, T.P. Harzer, V. Chawla, S. Djaziri, B. Phillipi, J. Wehrs, J.M. Wheeler, J. Michler, G. Dehm, Acta Mater. 93 (2015) 175–186.

[17] Y. Liu, D. Bufford, H. Wang, C. Sun, X. Zhang, Acta Mater. 59 (2011) 1924–1933.

[18] B.C. Kang, H.Y. Kim, O.Y. Kwon, S.H. Hong, Scripta Mater. 57 (2007) 703–706.

[19] A.F. Jankowski, J.P. Hayes, C.K. Saw, Phil. Mag. 87 (16) (2007) 2323–2334.

[20] B. Ham, X. Zhang, Mater. Sci. Eng. A. 528 (2011) 2028–2033.

[21] G.H. Yang, B. Zhao, Y. Gao, F. Pan, Surf. Coat. Technol. 191 (2005) 127–133.

[22] Q. Zhou, J.J. Li, F. Wang, P. Huang, K.W. Xu, T.J. Lu, Scripta Mater. 111 (2016) 123–126.

[23] J.Y. Zhang, X. Zhang, R.H. Wang, S.Y. Lei, P. Zhang, J.J. Niu, G. Liu, G.J. Zhang, J. Sun, Acta Mater. 59 (2011) 7368–7379.

[24] J.Y. Zhang, S. Lei, J. Niu, Y. Liu, G. Liu, X. Zhang, J. Sun, Acta Mater. 60 (2012) 4054–4064.

[25] Y.F. Sun, Y. Todaka, M. Umemoto, N. Tsuji, J. Mater. Sci. 43 (2008) 7457–7464.

[26] M. Callisti, T. Polcar, Acta Mater. 124 (2017) 247–260.

[27] W.Z. Han, M.J. Demkowicz, E.G. Fu, Y.Q. Wang, A. Misra, Acta Mater. 60 (2012) 6341–6351.

[28] X.M. Bai, A.F. Voter, R.G. Hoagland, M. Nastasi, B.P. Uberuaga, Science 327 (2010) 1631–1634.

[29] M.G. Ramezani, M.J. Demkowicz, G. Feng, M.P. Rutner, Scr. Mater. 139 (2017) 114–118.

[30] A.P. Zhilyaev, T.G. Langdon, Prog. Mater. Sci. 53 (2008) 893-979.

[31] B. Ahn, A.P. Zhilyaev, H.J. Lee, M. Kawasaki, T.G. Langdon, Mater. Sci. Eng. A. 638 (2015) 109–117.

[32] J.K. Han, H.J. Lee, J.I. Jang, M. Kawasaki, T.G. Langdon, Mater. Sci. Eng. A. 684 (2017) 318–327.

[33] J.K. Han, D.K. Han, G.Y. Liang, J.I. Jang, T.G. Langdon, M. Kawasaki, Adv. Eng. Mater. 20 (2018) 1800642(1-9).

[34] V.N. Danilenko, S.N. Sergeev, J.A. Baimova, G.F. Korznikova, K.S. Nazarov, R. Kh. Khisamov, A.M. Glezer, R.R. Mulyukov, Mater. Lett. 236 (2019) 51–55.

[35] N. Ibrahim, M. Peterlechner, F. Emeis, M. Wegner, S.V. Divinski, G. Wilde, Mater. Sci. Eng. A. 685 (2017) 19-30.

[36] J.K. Han, K.D. Liss, T.G. Langdon, M. Kawasaki, Sci. Reports 9 (2019) 17186(1-7).

[37] T.G. Langdon, Acta Mater. 61 (2013) 7035–7059.

[38] M. Knezevic, T. Nizolek, M. Ardeljan, I.J. Beyerlein, N.A. Mara, T.M. Pollock, Int. J. Plast. 57 (2014) 16–28.

[39] J.S. Carpenter, T. Nizolek, R.J. McCabe, M. Knezevic, S.J. Zheng, B.P. Eftink, J.E. Scott, S.C. Vogel, T.M. Pollock, N.A. Mara, I.J. Beyerlein, Acta Mater. 92 (2015) 97–108.

[40] J.S. Carpenter, T.J. Nizolek, R.J. McCabe, S.J. Zheng, J.E. Scott, S.C. Vogel, N.A. Mara, T.M. Pollock, I.J. Beyerlein, Mater. Res. Lett. 3 (2015) 50–57.

[41] M. Ardeljan, D.J. Savage, A. Kumar, I.J. Beyerlein, M. Knezevic, Acta Mater. 115 (2016) 189–203.

[42] K. Oh-ishi, K. Edalati, H.S. Kim, K. Hono, Z. Horita, Acta Mater. 61 (2013) 3482-3489.

[43] O. Bouaziz, H.S. Kim, Y. Estrin, Adv. Eng. Mater. 15 (2013) 336-340.

[44] C. Xu, Z. Horita, T.G. Langdon, Acta Mater. 56 (2008) 5168-5176.

[45] Y. Huang, T.G. Langdon, Mater. Today 16 (2013) 85-93.

[46] R.B. Figueiredo, P.R. Cetlin, T.G. Langdon, Mater. Sci. Eng. A. 528 (2011) 8198–8204.

[47] R.B. Figueiredo, P.H.R. Pereira, M.T.P. Aguilar, P.R. Cetlin, T.G. Langdon, Acta Mater. 60 (2012) 3190–3198.

[48] Y. Huang, R.B. Figueiredo, T. Baudin, F. Brisset, T.G. Langdon, Adv. Eng. Mater. 14 (2012) 1018-1026.

[49] P.R. Cetlin, M.T.P. Aguilar, R.B. Figueiredo, T.G. Langdon, J. Mater. Sci. 45 (2010) 4561-4570.

[50] R.B. Figueiredo, P.R. Cetlin, T.G. Langdon, Metall. Mater. Trans. A. 41A (2010) 778-786.

[51] R.Z. Valiev, Yu.V. Ivanisenko, E.F. Rauch, B. Baudelet, Acta Mater. 44 (1996) 4705-4712.

[52] M. Kawasaki, R.B. Figueiredo, T.G. Langdon, Acta Mater. 59 (2011) 308-316.

[53] Y. Estrin, A. Molotnikov, C.H.J. Davies, R. Lapovok, J. Mech. Phys. Solids 56 (2008) 1186-1202.

[54] Y. Huang, M. Kawasaki, T.G. Langdon, Adv. Eng. Mater. 15 (2013) 747-655.

[55] Y. Huang, M. Kawasaki, T.G. Langdon, J. Mater. Sci. 48 (2013) 4533-4542.

[56] Y. Huang, M. Kawasaki, T.G. Langdon, J. Mater. Sci. 49 (2014) 3146-3157.

[57] W. Jiang, X.H. An, S.D. Wu, Z.F. Zhang, R.B. Figueiredo, N. Gao, T.G. Langdon, Y. Zhu, Adv. Eng. Mater. 22 (2020) 1900477(1-8).

[58] R. Kulagin, Y. Beygelzimer, Y. Ivanisenko, A. Mazilkin, H. Hahn, IOP Conf. Series: Mater. Sci. Eng. 194 (2017) 012045(1-6).

[59] R. Kulagin, Y. Beygelzimer, Y. Ivanisenko, A. Mazilkin, B. Straumal, H. Hahn, Mater. Lett. 222 (2018) 172-175.

[60] R. Kulagin, Y. Beygelzimer, A. Bachmaier, R. Pippan, Y. Estrin, Appl. Mater. Today 15 (2019) 236-241.

[61] M. Pouryazdan, B.J.P. Kaus, A. Rack, A. Ershov, H. Hahn, Nature Commun. 8 (2017) 1611(1-7).

[62] T. Mousavi, J. Dai, P. Bazarnik, P.H.R. Pereira, Y. Huang, M. Lewandowska, T.G. Langdon, J. Alloys Compds 832 (2020) 155007(1-8).

[63] A. Heczel, M. Kawasaki, J.L. Lábár, J.I. Jang, T.G. Langdon, J. Gubicza, J. Alloys Compds 711 (2017) 141-154.

[64] M.V.P. Companhoni, J.R.G. Matheus, T.L.M Marcondes, A.L. Pinto, J. Mater. Sci 47 (2012) 7835–7840.

[65] S.O. Rogachev, A.B. Rozhnov, S.A. Nikulin, O.V. Rybal'chenko, M.V. Gorshenkov, V.G. Chzhen, S.V. Dobatkin, Phys. Metal. Metallog. 117 (2016) 371–377.

[66] S. Lee, Z. Horita, Mater. Trans. 53 (2013) 38–45.

[67] A.P. Zhilyaev, F. Gálvez, A. Sharafutdinov, M.T. Pérez-Prado, Mater. Sci. Eng. A. 527 (2010) 3918–3928.

[68] J. K. Han, J. Jang, T.G. Langdon, M. Kawasaki, Mater. Trans. 60 (2019) 1131-1138.

[69] D. Hernández-Escobar, Z. U. Rahman, H. Yilmazer, M. Kawasaki, C. J. Boehlert, Philos. Mag. 99 (2019) 557-584.

Figures captions

Fig. 1 OM micrographs of cross-sections of the Zr/Nb composites fabricated by HPT through (a) 10, (b) 20, (c) 50, (d) 80 and (e) 100 turns.

Fig. 2 Cross-sectional SEM images of the Zr/Nb composites fabricated by HPT through 50 turns: (a) edge (mixed area), (b) centre, (c) EDS distribution of Zr from central area, (d) EDS distribution of Nb from central area.

Fig. 3 Color-coded contour maps of the Vickers microhardness for the vertical cross-sectional planes after HPT for 10 to 100 turns.

Fig. 4 Bright field and dark field TEM images of the Zr/Nb samples: (a) and (b) centre after 80 turns, (c) and (d) centre after 100 truns, (e) and (f) edge after 100 turns.

Fig. 5 Diffraction patterns (upper) and equivalent grain size distributions (lower) for (a) centre after 80 turns, (b) centre after 100 turns, (c) edge after 100 turns, with (d), (e) and (f) as the corresponding grain size distributions.

Fig. 6 HR images and corresponding FFT patterns for (a) bcc Nb and (b) twinned hcp Zr in the edge region after 100 turns.

Fig. 7 EDS maps of the Zr/Nb composite after 100 turns for (a) centre and (b) edge.

Table caption

Table 1 Maximum Vickers hardness values reported for different materials after HPT processing.

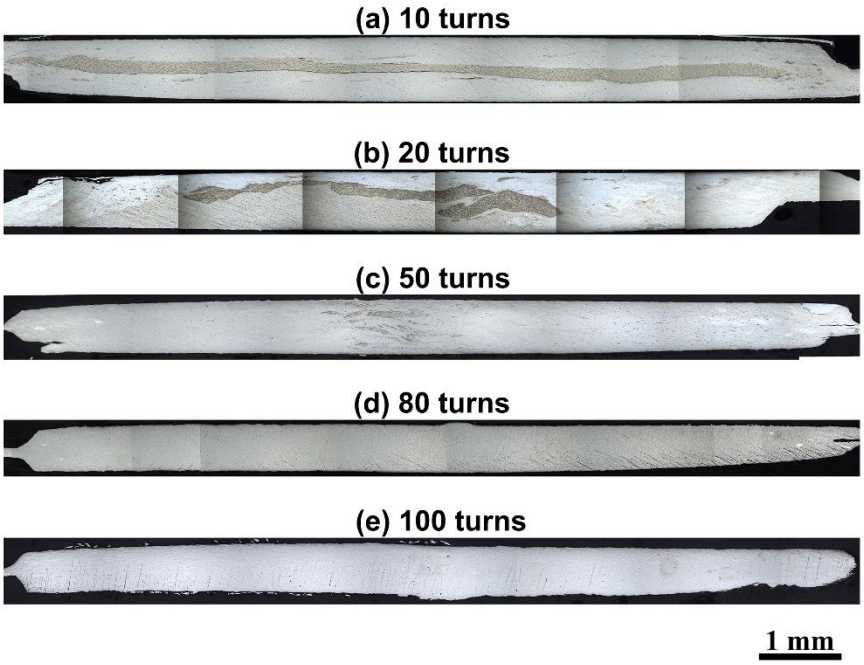

Fig. 1 OM micrographs of cross section of Zr/Nb composite fabricated by HPT through: (a) 10, (b) 20, (c) 50, (d) 80 and (e) 100 turns.

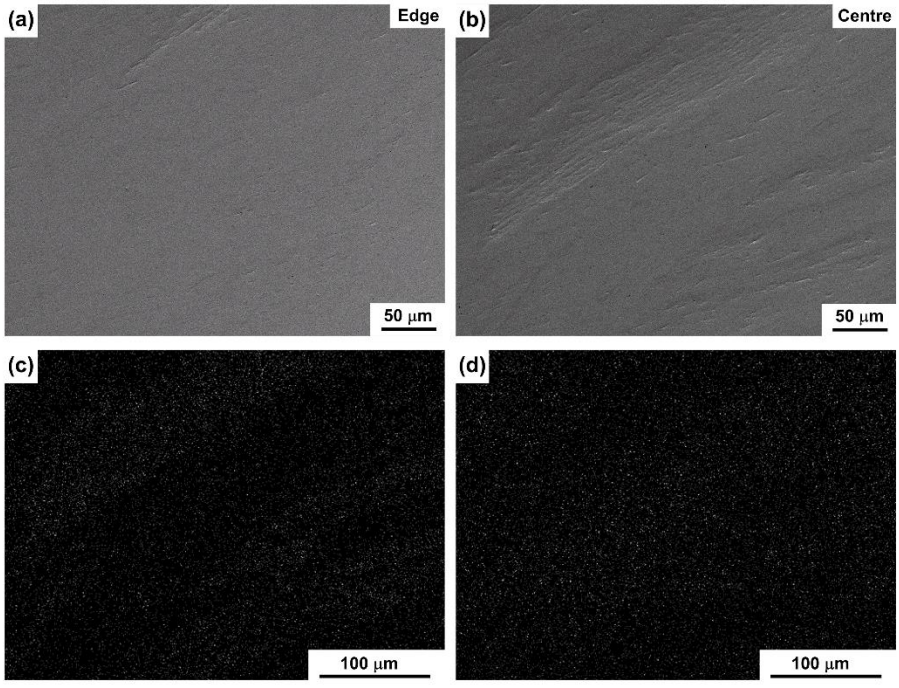

Fig. 2 Cross-sectional SEM images of the Zr/Nb composites fabricated by HPT through 50 turns: (a) edge (mixed area), (b) centre, (c) EDS distribution of Zr from central area, (d) EDS distribution of Nb from central area.

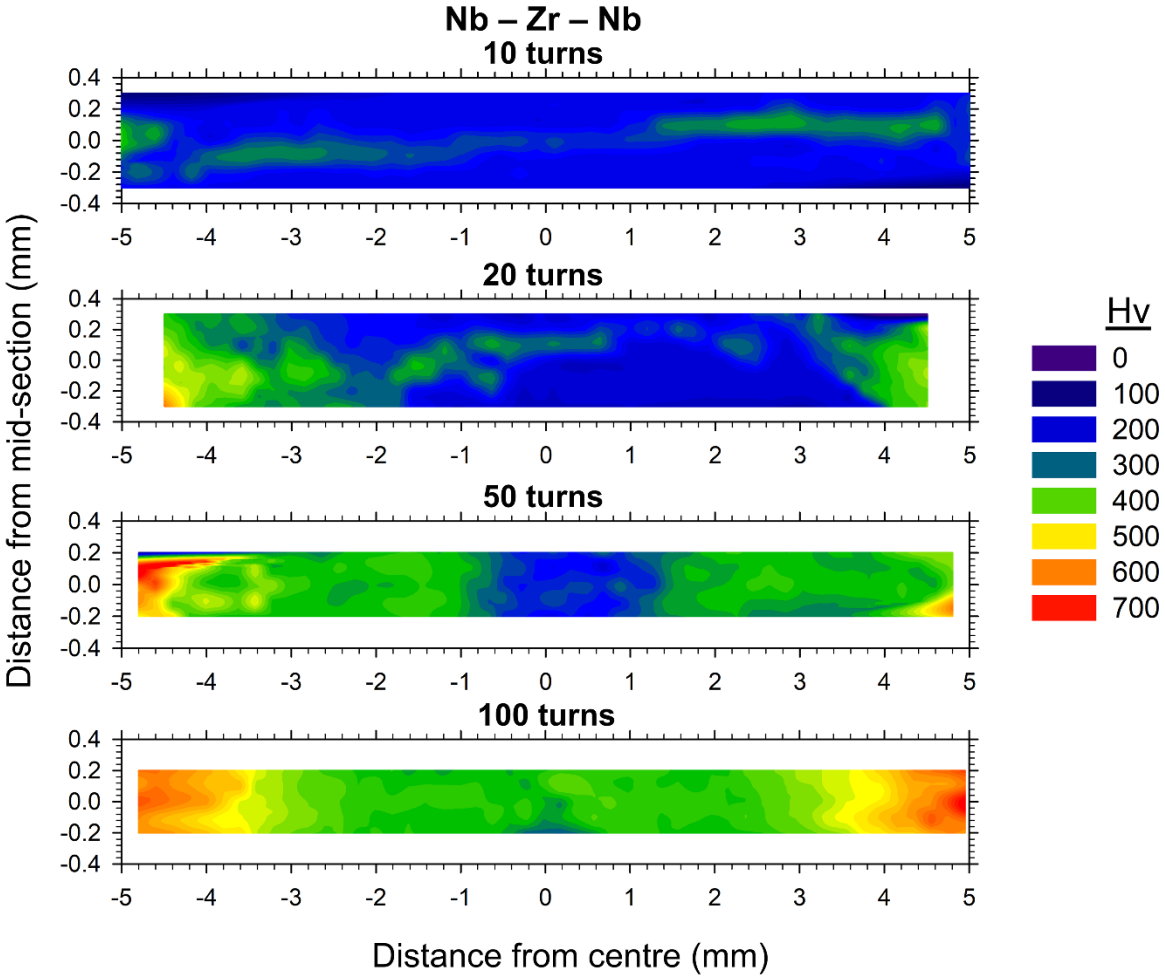

Fig. 3 Color-coded contour maps of the Vickers microhardness for the vertical cross-sectional planes after HPT for 10 to 100 turns.

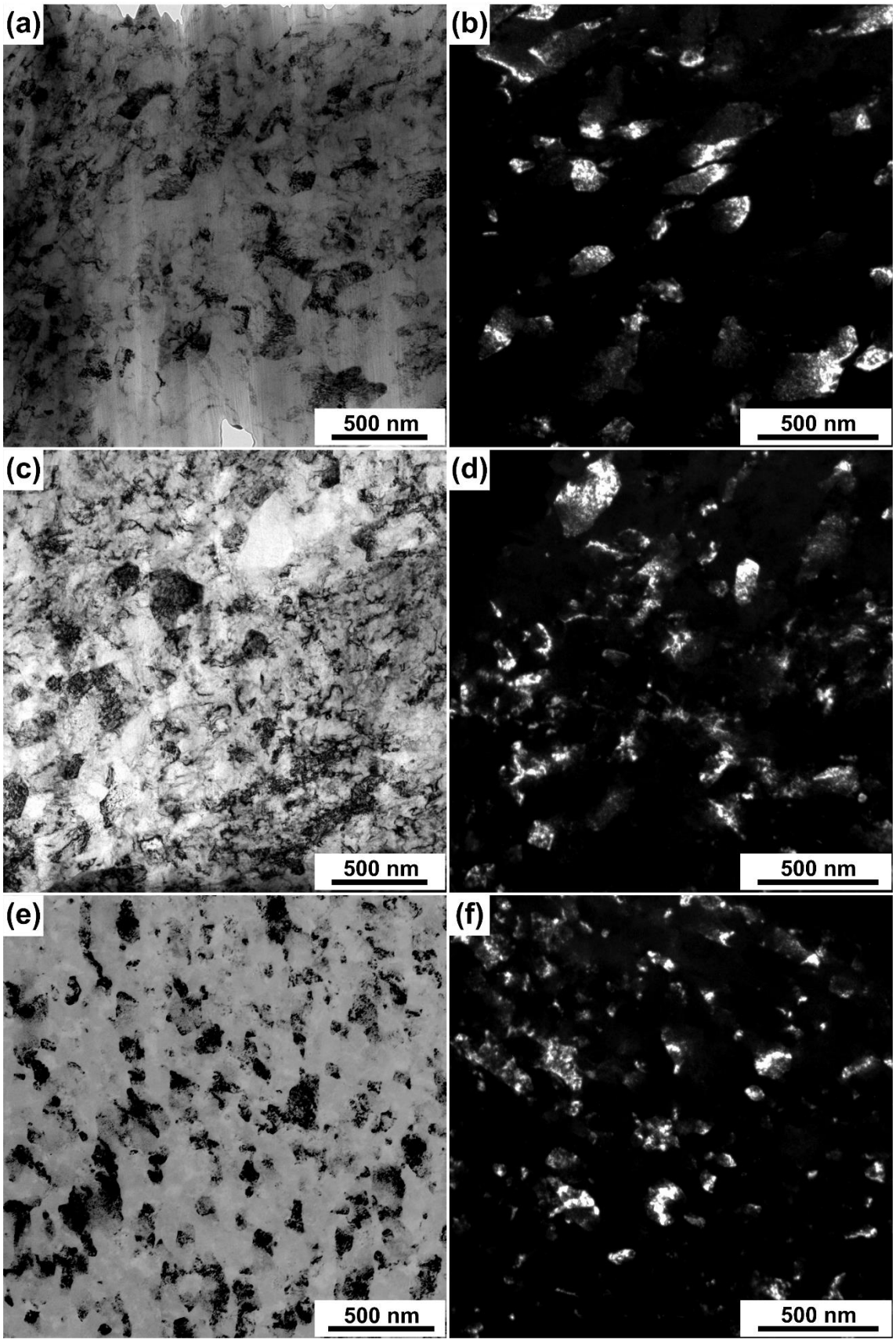

Fig. 4 Bright field and dark field TEM images of the Zr/Nb samples: (a) and (b) centre after 80 turns, (c) and (d) centre after 100 turns, (e) and (f) edge after 100 turns.

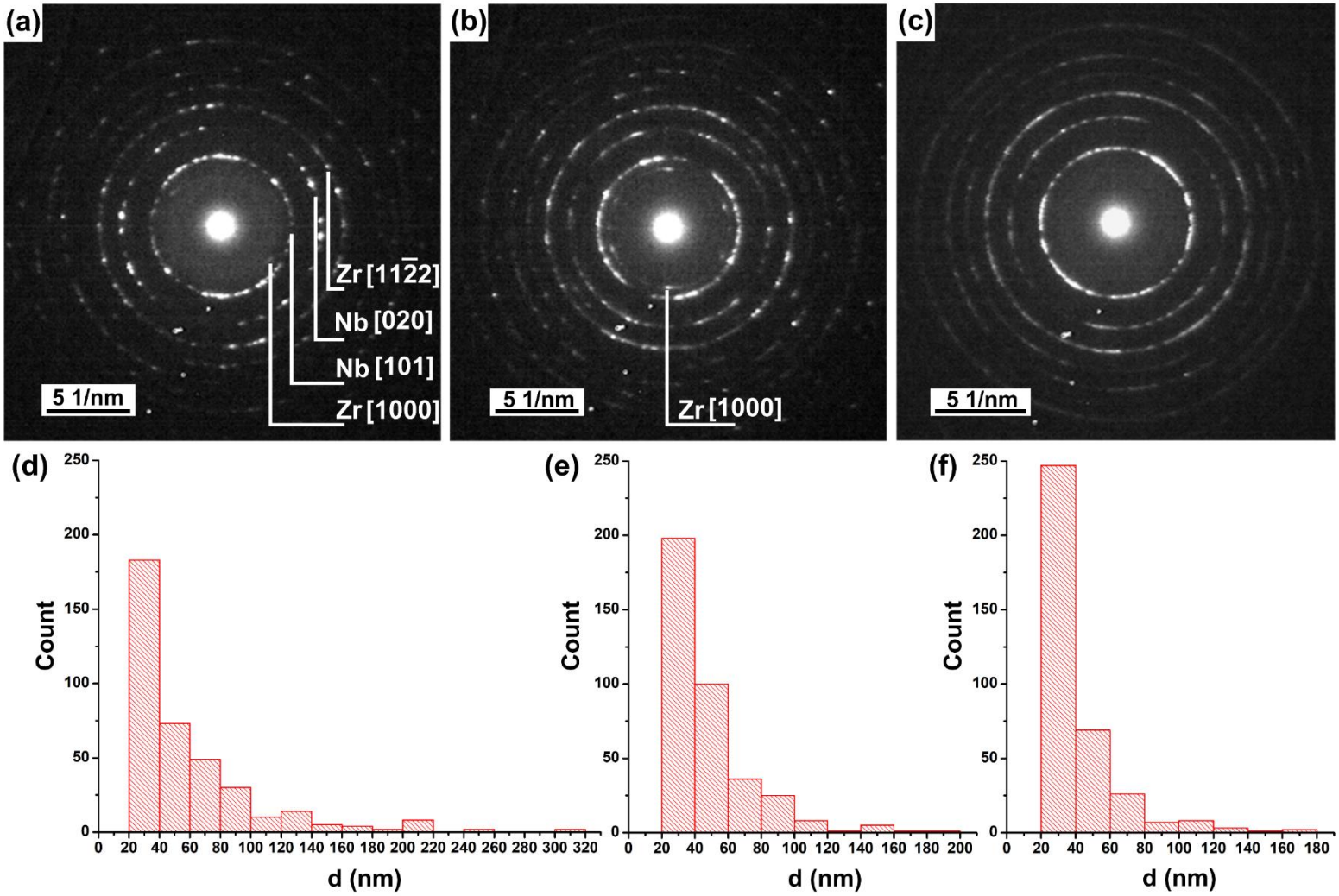

Fig. 5 Diffraction patterns (upper) and equivalent grain size distribution (lower) for (a) centre after 80 turns, (b) centre after 100 turns and (c) edge after 100 turns, with (d), (e) and (f) as the corresponding grain size distributions.

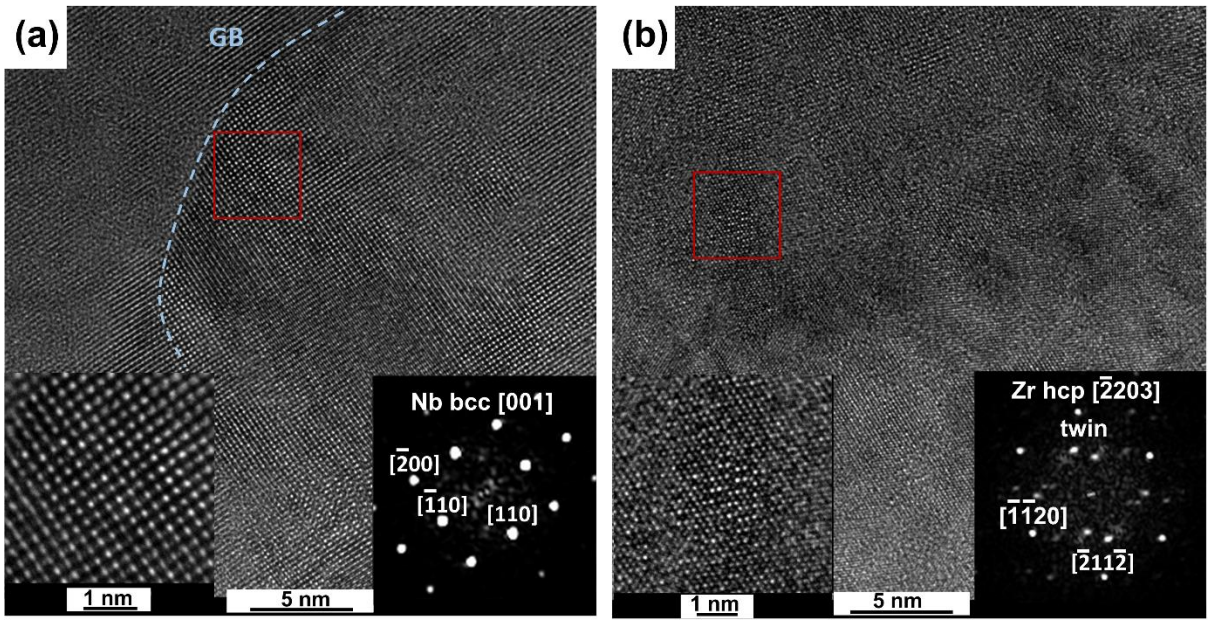

Fig.6 HR images and corresponding FFT patterns for a) bcc Nb and b) twinned hcp Zr in the edge region after 100 turns.

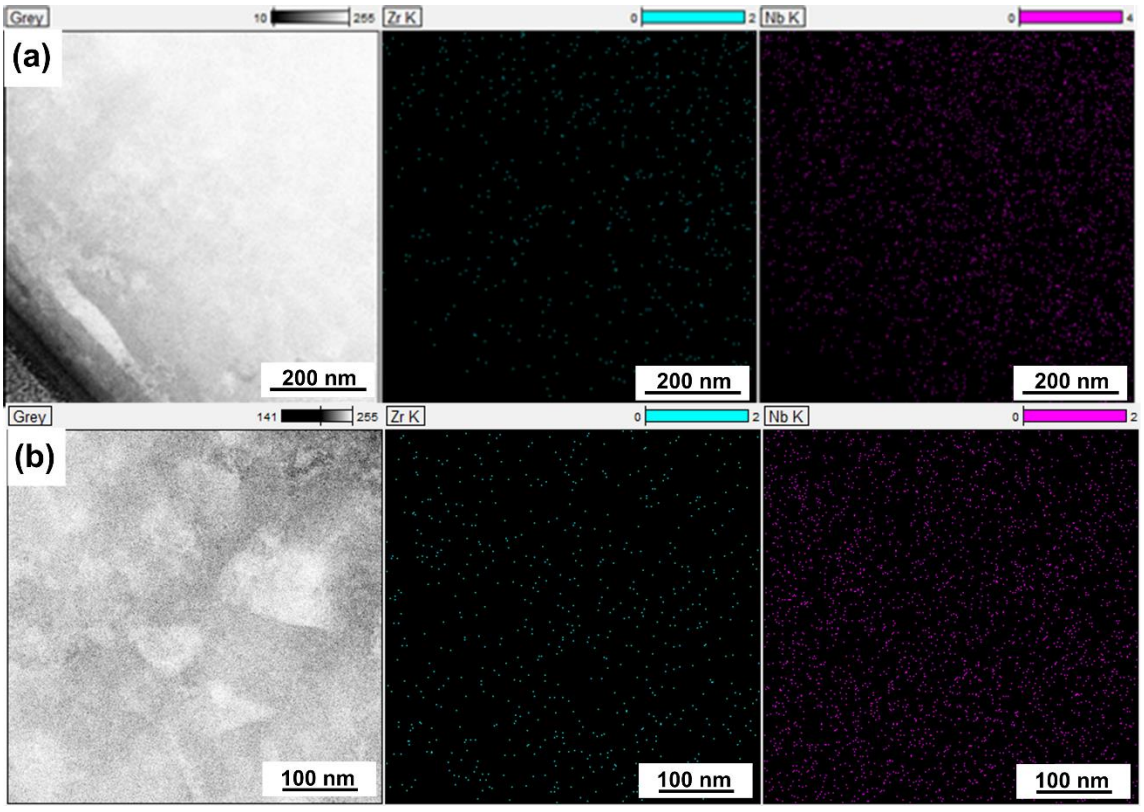

Fig. 7 EDS maps of the Zr/Nb composites after 100 turns for (a) centre and (b) edge.

Table 1. Maximum Vickers hardness values reported for different materials after HPT processing.

Material	Maximum Hardness (Hv)
Al/Mg (10 turns) [32]	270
Al/Mg (20 turns) [32]	330
Al/Mg (100 turns) [36]	370
Al/Cu (20-40 turns) [33]	400
Al/Cu (60 turns) [33]	500
Al/Fe (20 turns) [68]	320
CP Al (5 turns) [32]	65
ZK60 (5 turns) [32]	110
CP Cu (10 turns) [33]	150
CP Fe (10 turns) [68]	310
Mg/Zn (30 turns) [69]	250
Zr-Nb alloy (5 turns) [64]	470
Zr-Nb alloy (10 turns) [65]	385
Nb (5 turns) [66]	~230
Zr (5 turns) [67]	340
Zr/Nb (100 turns) [5]	~500
Zr/Nb (100 turns) This work	700